Antiferromagnetic FeTe₂ 1*T*-phase formation at the Sb₂Te₃/Ni₈₀Fe₂₀ interface

A. R. Will-Cole, ¹ James L. Hart, ² Matthew Matzelle, ³ Adrian Podpirka, ⁴ Nirjhar Bhattacharjee, ¹ Shreya K. Patel, ⁵ Sarah H. Tolbert, ⁵ Arun Bansil, ³ Judy J. Cha, ² Don Heiman, ^{3,6} and Nian X. Sun, ¹ Electrical and Computer Engineering, Northeastern University, Boston, Massachusetts 02115, USA, ² Materials Science and Engineering, Cornell University, Ithaca, New York 14853, USA, ³ Department of Physics, Northeastern University, Boston, Massachusetts 02115, USA, ⁴ Applied Physics Laboratory, Johns Hopkins, Laurel, Maryland 20723, USA, ⁵ Department of Chemistry and Biochemistry, University of California Los Angeles, Los Angeles, California 90095, USA, ⁶ Plasma Science and Fusion Center, Massachusetts Institute of Technology, Cambridge, Massachusetts 02139, USA



(Received 4 November 2022; revised 31 January 2023; accepted 1 February 2023; published 15 February 2023)

Bilayer topological insulator/ferromagnet (TI/FM) heterostructures are promising for spintronic applications due to their low switching energy and therefore power efficiency. Until recently, the reactivity of TIs with FM films was overlooked in the spin-orbit-torque literature, even though there are reports that it is energetically favorable for TIs to react with transition metals and form interfacial layers. In this study, we fabricated a TI/FM heterostructure comprised of molecular beam epitaxy grown Sb₂Te₃ and dc sputtered Ni₈₀Fe₂₀. Broadband ferromagnetic resonance revealed spin-pumping evident by the significant enhancement in Gilbert damping, which is likely a signature of the topological surface states or the presence of large spin-orbit coupling in the adjacent Sb₇Te₃. With low-temperature magnetometry, an exchange bias is observed that indicates an exchange interaction between an antiferromagnet (AFM) and an adjacent FM. Cross-section high-angle annular dark-field scanning transmission electron microscopy characterization of the Sb₂Te₃-Ni₈₀Fe₂₀ bilayer revealed a complex interface showing diffusion of Fe and Ni into the Sb₂Te₃ film yielding the formation of a FeTe₂ 1T-type structural phase. Furthermore, density functional theory calculations revealed that the FeTe₂ 1T-phase has an AFM ground state. Due to experimental limitations in the electron-energy-loss spectroscopy measurements, the precise chemistry of the interfacial phase could not be determined, therefore it is possible that the FeTe₂ 1T and/or an intermixed $(Fe_{1-x}Ni_x)Te_2$ 1T is the AFM interfacial phase contributing to exchange bias in the system. This work emphasizes the chemical complexity of TI/FM interfaces that host novel, metastable magnetic topological phases and require more in-depth studies of other similar interfaces.

DOI: 10.1103/PhysRevMaterials.7.024406

I. INTRODUCTION

Topological insulators (TIs), specifically $Bi_{1-x}Sb_x$ alloys and van der Waals (vdW) chalcogenides X_2Q_3 (X = Bi,Sb, Bi_1 _rSb_r; Q = Se, Te) with tetradymite structure, have insulating bulk state and two-dimensional metallic surfaces enabled by topologically protected Dirac surface states [1–3]. TIs exhibit large charge-to-spin conversion efficiencies, strong spin-momentum locking, and conductive surface states, making them ideal for applications in spin-orbit-torque magnetic random-access memory (SOT-MRAM) magnetic tunnel junction devices [4-10]. When magnetic order is introduced, time-reversal symmetry is broken, providing an energy gap in the surface states, and the electrons gain a net moment through short-range exchange interactions [11]. Magnetic TIs can exhibit exciting behavior such as the anomalous Hall effect, the quantum anomalous Hall effect, the topological magnetoelectric effect, and an axion insulator state [11–13]. Strategies to achieve magnetic order in TI include compositional doping, intrinsic magnetic TI, or proximity-induced magnetization (PIM) [14–18]. PIM can be achieved through growing magnetic insulator (MI) films directly on the TI surface [17-21].

For spin-orbit-torque devices based on TIs coupled with ferromagnets (FMs), there remain integration feasibility considerations such as interfacial orbital hybridization, novel interfacial chemical phases, etc. However, this is often overlooked or not mentioned in the literature on spin-pumping in these TI/metallic FM heterostructures [9,22,23]. There have been theoretical studies on the interface between TIs and metal contacts, namely Au/Bi₂Se₃ and graphene/Bi₂Se₃, which retain spin-momentum locking of the surface states, while Pd and Pt strongly couple to Bi₂Se₃ and cause delocalization of the surface states and less efficient spin-momentum locking [24]. Additionally, experiments confirm that band bending occurs at the Bi₂Se₃/metallic interface due to variation in the electron affinity of Bi₂Se₃ (4.45 eV) and work functions of transition-metal contacts (\sim 5 eV) [25]. The formation of interfacial layers in Bi₂Se₃/metal contacts and Bi₂Se₃/magnetic materials has been confirmed with x-ray photoelectron spectroscopy, and aside from Au (which was found to be inert), the metals were ranked by reaction strength (determined by the amount of Bi₂Se₃ consumed) as follows: Pd < Ir < Co < CoFe < Ni < Cr < NiFe < Fe [26].

More recently, novel materials have been found at the interfaces in TI/FM structures generated by interdiffusion

and subsequent reactions. Ni diffusion in Ni₈₀Fe₂₀/Bi₂Se₃ heterostructures resulted in a ternary magnetic phase of Ni:Bi₂Se₃ [27]. Further study of the Bi₂Te₃/Ni₈₀Fe₂₀ interface resulted in the discovery of the intrinsic antiferromagnetic (AFM) NiBi₂Te₄ [28]. This unique material has a Néel temperature of $T_N = 63$ K, which is significantly higher than that reported for the intrinsic antiferromagnetic topological insulator [28] MnBi₂Te₄, which has $T_N = 25$ K [16]. The discovery of NiBi₂Te₄ at the interface of Bi₂Te₃/Ni₈₀Fe₂₀ revealed that novel magnetic topological phases can exist at the interfaces, and thus these reactive TI interfaces can be used as a testbed for the discovery of stable and metastable quantum materials [28].

The goal of our study is to investigate the TI/FM heterostructure and interface of Sb₂Te₃/Ni₈₀Fe₂₀, where the Sb₂Te₃ is epitaxially grown by molecular beam epitaxy (MBE) on GaAs substrate. The FM, Ni₈₀Fe₂₀, is sputterdeposited on the Sb₂Te₃ film. We provide evidence that a novel AFM phase forms at the interface, which is structurally consistent with FeTe₂ 1T-phase (similar to the NiTe₂-type structure, specifically $P\bar{3}m1$). Additionally, our theoretical calculations indicate that the FeTe₂ 1T-phase has an AFM ground state, which is supported by an exchange bias observed in our magnetometry measurements. This FeTe₂ phase is a magnetic transition-metal dichalcogenide (TMD) with the chemical structure XY_2 comprised of transition-metal and chalcogen elements (X = Fe, Ni, W, Pd, etc.; Y = S, Se, Te, etc.)—these materials have been extensively studied since TMDs were proposed to host type-II Dirac fermions [29,30]. Experimentally, there have been two recent studies on the FeTe₂ 1T-phase—this phase has been stabilized in the form of nanoflakes via chemical vapor deposition [31], and in the form of single crystals [32]. Neither of these studies explicitly reports the presence of AFM order, however in the singlecrystal investigation an isostructural transition was observed with x-ray diffraction accompanied by a sharp decrease in magnetization, which was attributed to the presence of AFM coupling [32].

II. EXPERIMENTAL RESULTS AND DISCUSSION

In this study, we fabricated a Sb₂Te₃/Ni₈₀Fe₂₀ bilayer heterostructure on a GaAs substrate via a combinational growth regime. First, 10-nm-thick Sb₂Te₃ was epitaxially grown with molecular beam epitaxy (MBE) on a GaAs (100)-oriented substrate and capped with Te [33]. To confirm the crystalline quality of the Sb₂Te₃ film, high-angle, out-of-plane x-ray diffraction (XRD) was performed. The XRD pattern for the Sb₂Te₃ sample shown in Fig. 1(a) demonstrates the anticipated tetradymite crystal structure. The XRD pattern confirms a highly c-axis oriented growth of the TI film, as is evident by the presence of (00l)-peaks in the diffraction pattern. The rocking curve can be found in S1 of the Supplemental Material, and it shows that MBE-grown TI on a lattice-matched substrate has higher crystal quality than comparably sputtered TI on an amorphous substrate [28,34]. Additionally, crosssection high-angle annular dark-field scanning transmission electron microscopy (HAADF-STEM) imaging revealed further evidence of the vdW structure of the Sb₂Te₃ film—shown in Fig. 1(b). The TI growth on the GaAs

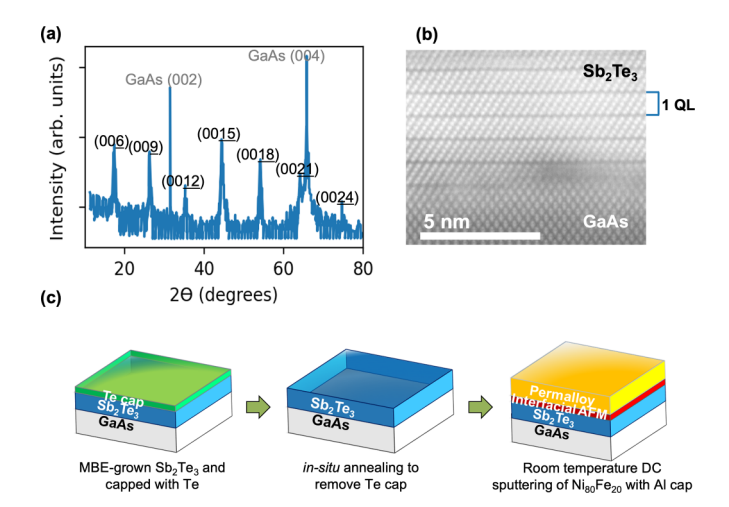


FIG. 1. (a) X-ray diffraction spectra of Sb₂Te₃/GaAs with labeled diffraction peaks. Peaks labeled with gray font correspond to the GaAs substrate, and black font labeled peaks correspond to the Sb₂Te₃ film. (b) High-angle annular dark-field scanning transmission electron microscopy cross-section image with GaAs and Sb₂Te₃ in view. The quintuple layer van der Waals structure is highlighted with each quintuple layer corresponding to approximately 1 nm thick. (c) The fabrication process flow is highlighted here, specifically the MBE growth of TI, Te-cap removal, and magnetic film deposition.

(100)—oriented substrate is slightly disordered for the first quintuple layer, likely due to the symmetry mismatch of the film to the substrate. However, by the second quintuple layer, the anticipated vdW tetradymite crystal structure can be seen for the Sb₂Te₃ film. Subsequent to the MBE-growth of Sb₂Te₃, vacuum was broken and the films were transferred into the sputtering chamber. The Te cap was removed with an in situ sublimation process consistent with methods established in the literature [35]. After cooling the sample to room temperature and achieving a base vacuum of less than 1.0×10^{-7} Torr, a 15 nm Ni₈₀Fe₂₀ (also known as permalloy, referred to as Py in the rest of the text and upcoming figures) film was dc sputtered at a power of 50 W. This was followed by a dc sputtered Al-cap of 2 nm on the film surface to prevent undesirable oxidation of the magnetic film. The fabrication process flow is provided in Fig. 1(c).

We performed room-temperature broadband ferromagnetic resonance (FMR) spectroscopy to confirm spin-pumping in the Sb₂Te₃/Py heterostructure samples. In the broadband FMR measurement at resonance, the Py magnetization precession acts as a source of angular momentum, and since Sb₂Te₃ acts as a spin sink due to its large spin-orbit-coupling and/or the presence of topologically protected surface states (TSSs), this leads to spin pumping (generation of spin current) across the interface into the Sb₂Te₃ layer—a schematic of the spin-pumping phenomenon is provided in Fig. 2(a). Therefore, there is a loss in angular momentum in the Py due to spin pumping across the interface. Spin pumping results in a significant enhancement in the Gilbert damping parameter, α , in the Sb₂Te₃/Py samples compared to a control sample of Py. Magnetic field sweep FMR measurements of Sb₂Te₃/Py and a control sample of Si/Al/Py/Al yielded the differential absorption spectra at each frequency (f) and only one derivative peak

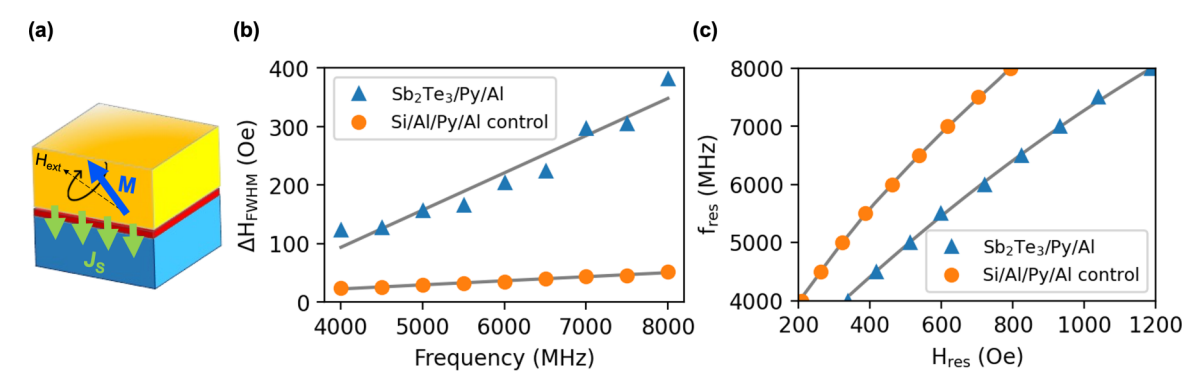


FIG. 2. (a) Schematic of spin-pumping. (b) Uniform mode resonance linewidth vs frequency with linear fit described by Eq. (1) to extract the Gilbert damping constant. (c) Frequency vs uniform mode resonance field with Kittel fit to extract effective in-plane magnetization.

was observed, which is the main resonance uniform mode. The Gilbert damping constant was extracted from a linear fit to the $\Delta H/\Delta f$ as a function of frequency using the relation provided in Eq. (1), where $\Delta H_{\rm FWHM}$ is the uniform mode linewidth, ΔH_0 is the inhomogeneous linewidth broadening, and γ is the gyromagnetic ratio (2.8 MHz/Oe for magnetic films) [36],

$$\Delta H_{\rm FWHM} = \Delta H_0 + \frac{2\pi\alpha}{\gamma}.$$
 (1)

The FMR results for Sb₂Te₃/Py and Si/Al/Py/Al are shown in Fig. 2(b), and the extracted α damping parameter is shown in Table I. As shown in Table I, there is giant enhancement in the Gilbert damping for the Sb₂Te₃/Py bilayer (an order of magnitude higher than the Si/Al/Py/Al control sample). This can be attributed to the TSS or the presence of large spin-orbit-coupling in the Sb₂Te₃ layer (likely the latter as the Sb₂Te₃ bulk conduction channels are not suppressed) [37–40]. The effective in-plane magnetization, $4\pi M_{\rm eff}$, was further extracted using the Kittel equation provided in Eq. (2), where $H_{\rm res}$ is the resonance field, and γ is the gyromagnetic ratio (2.8 MHz/Oe for magnetic materials),

$$f = |\gamma/2\pi| \sqrt{H_{\text{res}}(H_{\text{res}} + 4\pi M_{\text{eff}})}.$$
 (2)

The results are shown in Fig. 2(c), and the extracted $4\pi M_{\rm eff}$ is shown in Table I. There is a reduction in the $4\pi M_{\rm eff}$ between the Si/Al/Py/Al control and the Sb₂Te₃/Py heterostructure, which likely indicates out-of-plane canting leading to an out-of-plane magnetic component in the Py film or a reduction in magnetization of the FM film (this result is directly compared to the hysteresis loops in S2 of the Supplemental Material) [34]. Regardless, the Gilbert damping enhancement is indicative of spin-pumping in the Sb₂Te₃/Py bilayer system.

The reduction in $4\pi M_{\rm eff}$ between the Si/Al/Py/Al control and the Sb₂Te₃/Py heterostructure may indicate that there

TABLE I. Broadband FMR measurement results.

	α	$4\pi M_{ m eff}$
Si/Al/Py/Al	0.019	9.54 kG
Sb ₂ Te ₃ /Py	0.178	5.77 kG

is a reduction in magnetization rather than just the possibility of out-of-plane canting, so to further study the magnetic phases present, we measured the static, in-plane magnetic properties for the Sb₂Te₃/Py heterostructure as a function of decreasing temperature using a superconducting quantum interference device (SQUID) magnetometer. Magnetic hysteresis loop measurements revealed a large exchange bias $(H_{\rm EB} \sim 100\,{\rm Oe})$ present at low temperature $(T=6\,{\rm K})$ with +1 T and -1 T field cooling as shown in Fig. 3(a) compared with the room-temperature $(T = 300 \,\mathrm{K})$ hysteresis loop. The exchange bias effect is observed in coupled FM/AFM materials, and it arises due to uniaxial magnetic anisotropy induced at the interface between the two layers [41]. Our Fig. 3 suggests FM/AFM coupling is present here, and since the Sb₂Te₃ is nonmagnetic and the Py film is FM, we conclude that there is an interfacial AFM layer between Sb₂Te₃ and Py. In addition to the presence of the large exchange bias, we observe an accompanying increase in the Py coercive field, H_C , from ~4.25 Oe at T = 300 K to ~113.5 Oe (~94 Oe) at T = 6 K for 1 T (-1 T) field-cooling condition. The exchange interaction between FM and AFM not only causes exchange bias, but it also leads to a significant increase in coercive field possibly due to domains at a magnetically frustrated interface [28]. We also explored the magnitude of the exchange bias effect as a function of different field-cooling conditions, which is displayed in Fig. 3(b)—we observe a negative exchange bias effect, such that the hysteresis loops are shifted oppositely to the applied field-cooling direction. Temperature-resolved magnetometry was used to identify the Néel transition temperature (T_N) for the AFM. The magnetic moment was measured as a function of temperature with +1 T field cooling and zero field cooling for the Sb₂Te₃/Py heterostructure as shown in Fig. 3(c). The derivative of the moment with respect to the temperature is taken to identify the Néel temperature, and it is shown in Fig. 3(d). The Néel temperature is found to be $T_N = 40$ K—this is significantly higher than the most well-studied intrinsic topological antiferromagnet, MnBi₂Te₄, with $T_N \sim 20$ –25 K [16,42]. However, it is lower than $T_N = 63$ K for recently discovered NiBi₂Te₄ at a Bi₂Te₃/Py interface [28]. Finally, to confirm that $T_N = 40$ K corresponds to the onset of exchange bias in the Sb₂Te₃/Py heterostructure, temperature-dependent m(H) hysteresis loops were measured between 6 and 50 K. As shown in Fig. 4(a), the exchange bias effect is no longer observed by 50 K as

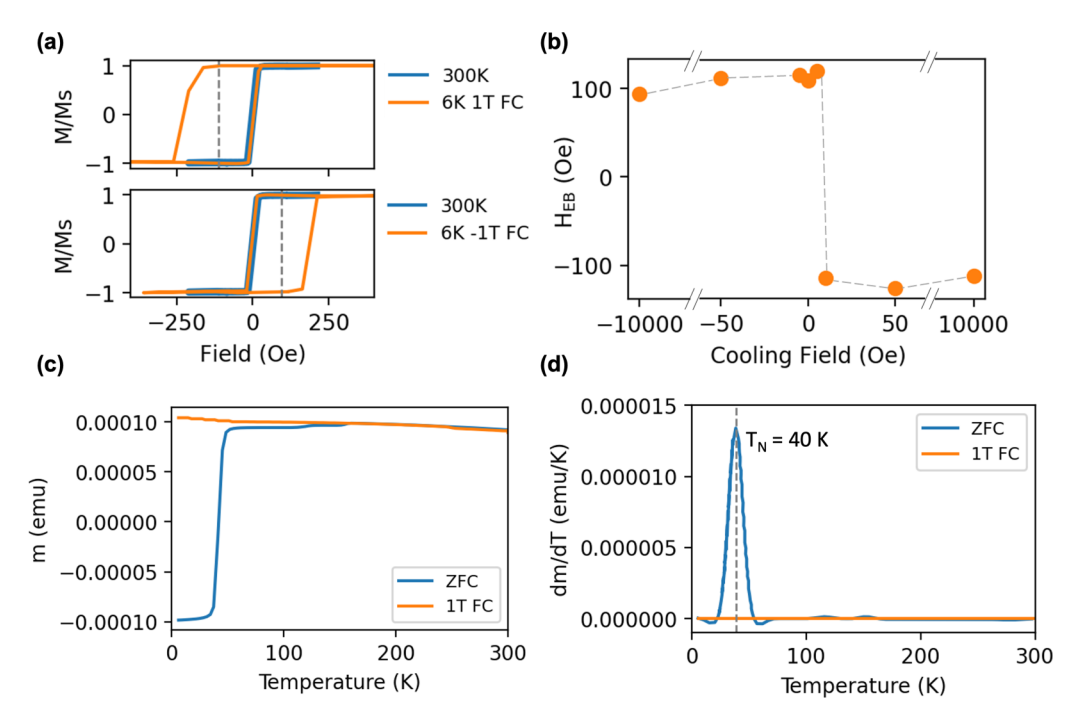


FIG. 3. (a) Magnetic hysteresis loop at 300 and 6 K for Sb₂Te₃/Py with +1 T field cooling (top) and 300 and 6 K for Sb₂Te₃/Py with -1 T field cooling (bottom). The gray dashed line represents the exchange bias field H_{EB} . (b) The H_{EB} plotted as a function of field-cooling condition. (c) Moment as a function of temperature for +1 T field cooled (FC) in orange and zero field cooled (ZFC) in blue. (d) Derivative of moment with respect to temperature for +1 T FC in orange and ZFC in blue. The gray dashed line is simply to highlight the Néel temperature, $T_{N} = 40 \text{ K}$.

evident by a centered, magnetic hysteresis loop with a narrow H_C . At 40 K, we observe a shift in the magnetic hysteresis loop indicative of a finite exchange bias. Additionally, below 40 K the H_C dramatically increases, which also supports the presence of exchange coupling and/or magnetic frustration, i.e., pinned domains. As temperature decreases, the $H_{\rm EB}$ and H_C both increase as summarized in Figs. 4(b) and 4(c), re-

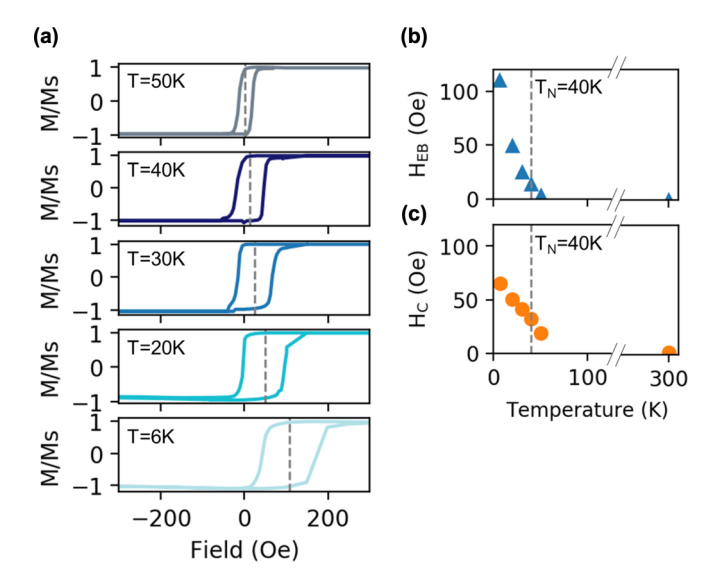


FIG. 4. (a) Magnetic hysteresis loop at 50, 40, 30, 20, and 10 K for Sb_2Te_3/Py with -1 T field cooling. (b) The exchange bias H_{EB} plotted as a function of temperature. (c) The coercive field plotted as a function of temperature.

spectively. This giant H_C enhancement and the presence of $H_{\rm EB}$ disappear at, or close to, the experimentally identified AFM Néel temperature, thus the interfacial AFM phase is responsible for this observed magnetic anisotropy [40]. The observed exchange bias was completely suppressed with the implementation of a Te spacer layer (data found in S3 of the Supplemental Material) [34]. Therefore, the Te alone is not reactive enough to form the interfacial AFM phase with Py, unlike the Sb₂Te₃/Py interface presented here. Besides the presence of exchange bias, there is evidence of magnetic frustration in the system. The irreversibility/bifurcation of the FC/ZFC curves in Fig. 3(c) at around 100 K may indicate that there is some additional magnetic frustration at the interface. The accompanying exponential decay of the coercivity with temperature shown in Fig. 4(c) may also point to magnetic frustration. The observed signatures of this magnetic frustration may arise due to additional disorder at the interface.

The observed exchange bias in the Sb_2Te_3/Py system is due to an interfacial AFM phase at the interface, analogous to what was reported in the Bi_2Te_3/Py system with an interfacial topological AFM $NiBi_2Te_4$ phase [28]. To investigate the accurate morphology and composition of the interfacial AFM phase, we performed cross-section HAADF-STEM. Focused ion-beam (FIB) milling was used to make the cross-section sample, and the FIB lift-out had a surface normal of GaAs [011]. As shown in Fig. 5(a), the interface between Sb_2Te_3 and Py is complex and disordered, with a high concentration of defects and nanoscale crystalline structures distinct from the Sb_2Te_3 tetradymite structure. The interfacial reaction has partially consumed the Sb_2Te_3 film and has resulted in a thickness

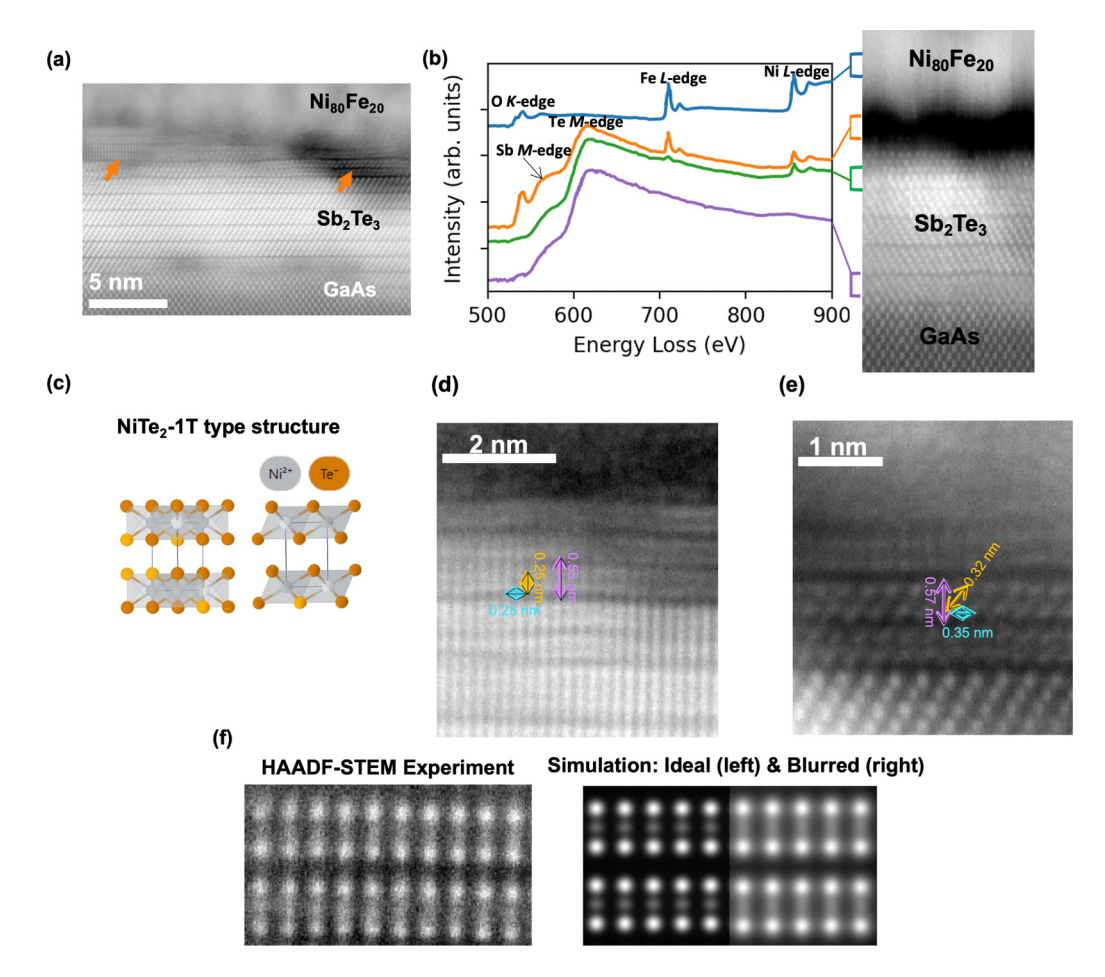


FIG. 5. (a) Representative HAADF-STEM cross-section image. Orange arrows point to the interfacial phase. (b) Representative STEM EELS spectra with corresponding STEM image. The colors and lines are a guide to where in the cross-section the data were collected. (c) Atomic models of the NiTe₂-type structure in the two common orientations observed at the interface. The structure was retrieved from the Materials Project for NiTe₂ (mp-2578) ($P\bar{3}m1$) from database version v2021.11.10. (d) Zoomed-in HAADF-STEM cross-section image of the orientation on the left in (c). (e) Zoomed-in HAADF-STEM cross-section image of the orientation on the right in (c). (f) Experimental HAADF-STEM image of the interfacial NiTe₂-type structure [zoomed-in further than (d)]. (g) Simulated HAADF-STEM image using COMPUTEM package with and without blurring (right and left, respectively).

variation of the Sb₂Te₃ (5–7 QLs) across the heterostructure. The predominant interfacial structure has an out-of-plane lattice constant of 0.5 nm, roughly half that of the Sb₂Te₃ QL. Electron-energy-loss spectroscopy (EELS) was performed at different sections through the thickness of the heterostructure. The EELS spectra are shown in Fig. 5(b). Note there is oxidation present in the sample based on the prevalence of the oxygen K-edge which is attributed to the fact that the sample was stored in atmosphere post-FIB lift-out. The presence of the Fe-L edge and Ni-L edge in the disordered interfacial region (orange) and the ordered interfacial phase region (green) indicates that there is diffusion of Fe and Ni into the Sb₂Te₃ film during the room-temperature sputter deposition of the Py film. This diffusion is followed by an interfacial reaction resulting in an interfacial phase seen in Sb₂Te₃/Py, promoted by the TSS electrons on the Sb₂Te₃ surface. The interfacial phase is consistent with a NiTe₂-type structure, specifically $P\bar{3}m1$ [structure retrieved from the Materials Project for NiTe₂] (mp-2578) from database version v2021.11.10] [43]. For the orientation that is shown in Fig. 5(d), the out-of-plane layer spacing is 0.55 nm, the in-plane bond distance is 0.2 nm, the out-of-plane bond distance is 0.25 nm, and the bond angle is 90°. For the orientation shown in Fig. 5(e), the out-ofplane layer spacing is 0.57 nm, the in-plane bond distance is 0.35 nm, the out-of-plane bond distance is 0.32 nm, and the bond angle is 55° (estimated error in the bond lengths is 0.03 nm). It is important to note that in HAADF-STEM imaging heavier elements correspond to higher intensity, therefore in the images shown in Fig. 5 the bright atoms correspond to the Te-sites. Shown in Fig. 5(f) is the NiTe₂-type interfacial structure with both the Ni- and Te-sites resolved in the image. This HAADF-STEM image was compared to a simulated HAADF-STEM image for the NiTe₂, which appears to be visually and qualitatively consistent [43]. The simulated HAADF-STEM image [shown in Fig. 5(g)] was generated using Kirkland's COMPUTEM package [44]. There are more STEM images in S4 of the supplemental material—these include other instances of the NiTe₂ 1T-like structure and other indications of disorder, specifically stacking fault defects near the interface. We note that the in-plane size of the interfacial domains (<10 nm) is significantly less than the thickness of the STEM specimen. Thus, when the STEM probe is placed over the crystalline interfacial phase shown Fig. 5, the probe is likely also passing through the amorphous Py and/or another disordered phase. Thus, we cannot determine the composition of the interfacial NiTe₂-like phase, but we note that the Ni, Fe, Te, and Sb are all detected within this region, thus they may be present within this interfacial phase with NiTe₂ 1*T*-like structure. Therefore, we pursued theoretical calculations to better understand what possible compositions contribute to the AFM phase.

III. THEORETICAL RESULTS AND DISCUSSION

Following the experimental results, density functional theory calculations were required to definitively identify the AFM interfacial phase. The magnetometry data and the presence of exchange bias in the heterostructure strongly suggest that there should be an AFM phase in contact with the FM Py at the Sb₂Te₃/Py interface. Based on the STEM-EELS data, there is Fe and Ni diffusion in the interfacial phase region, therefore the chemical composition of the interfacial region must include Fe and/or Ni. To determine the most probable AFM phase, first-principles calculations were carried out using projector augmented-wave pseudopotentials implemented by the Vienna *ab initio* simulation package (VASP) [45–49]. In previous theoretical studies on the NiTe₂ 1T-phase, calculations using the functionals of LDA+U and PBE+U found distinctly different, nonmagnetic solutions compared to those calculations employing hybrid functionals [50]. Therefore, the presence of correlation effects is important for elucidating the magnetic ground state of the NiTe₂ 1T-phase, which led to the choice of the SCAN functional as has been shown to be successful at incorporating correlation effects overlooked using the PBE or LDA (even without including the U parameter) [51-53]. Here, an energy cutoff of 520 eV was used and the Brillouin zone was sampled by a Γ -centered grid with points evenly spaced at most 0.07/Å apart. The lattice parameters and atomic positions were relaxed with the conjugate gradient method until the forces in the unit cell were less than 0.008 eV/Å and self-consistency was reached when the energy difference between the electronic steps was less than 10^{-7} eV. Again, based on the STEM-EELS data there is Fe and Ni diffusion into the Sb₂Te₃ film, therefore the chemical composition in the interfacial AFM phase must be a combination of Ni, Fe, Sb, and/or Te. The interfacial crystal structure in the high-resolution HAADF-STEM images closely resembles XY_2 1T-phase (X = Ni,Fe and Y = Te,Sb), but we are not ruling out the XY_2 2H-phase in our calculations. Additionally, we have included materials with space group 194 and atomic formula XY. We performed first-principles calculations on the possible combinations of X and Y elements in these three structures $(XY_2 \ 1T, XY_2 \ 2H, \text{ and } XY)$. First, we tested for stable magnetic solutions with any magnetic moments on the unit cell equal to or larger than 0.01 μ_B . Although we cannot make a direct comparison between our bulk calculations employing the SCAN functional with the aforementioned hybrid functional calculations of monolayers, the total magnetic moments should be similar. We found moments of 2.04 $\mu_{\rm B}$ and $0.08 \mu_B$ for FeTe₂ 2H and NiTe₂ 1T, respectively, which is consistent with the $2.00 \,\mu_{\rm B}$ and $0.11 \,\mu_{\rm B}$ reported in Ref. [50]. These results are summarized in Table II.

TABLE II. Presence of stable magnetic solutions. The magnetic moments on the unit cells are given in units of $\mu_{\rm B}$.

	Sb	Sb ₂ 1 <i>T</i>	Sb ₂ 2H	Te	Te ₂ 1 <i>T</i>	Te ₂ 2H
Fe	3.87	2.27	2.57	4.90	2.38	2.04
Ni	0.00	0.00	0.00	0.00	0.08	0.00

For materials identified to have stable magnetic solutions, we then performed supercell calculations using the lattice constants and atomic positions optimized in the primitive unit cell. For the XY structure there are two X-atomic sites in the primitive cell—thus, the out-of-plane (OP) AFM solution was calculated for the XY primitive cells. For the XY_2 structures, a $1 \times 1 \times 2$ supercell was used to calculate the energy of OP AFM solutions. For the XY, XY_2 1T, and XY_2 2H structures, a $2 \times 2 \times 1$ supercell was used to calculate the energy of the in-plane (IP) AFM solutions. Note, the three IP AFM arrangements that are possible in the $2 \times 2 \times 1$ supercell are all equivalent due to the threefold symmetry, therefore we only record one solution. The energy differences between these equivalent states are less than 0.01 meV. If a given material's ground state is AFM, then the FM state must be higher in energy than the AFM state. In Table III the results are summarized with the recorded energy differences between the lowest-energy state for each structure and formula with the IP and OP AFM, FM, and the nonmagnetic (NM) states. While NiTe₂ 1T-phase was a possible candidate for the AFM interfacial phase based on the structural similarities identified in the HAADF-STEM images and previous reports of antiparallel moments between Ni and Te sites in the literature [50], the NiTe₂ 1T-phase showed no stable AFM solutions in our calculations. Specifically, when magnetic moments were initialized with antiparallel moments between the Ni-sites, the final solution after self-consistency was always NM.

Out of the candidate materials, only the FeSb and FeTe₂ 1*T*-phase were found to have AFM ground states. Their ground state is characterized by an intraplanar "stripe" -like AFM coupling and interplanar FM coupling—this is depicted in Fig. 6. While there are no studies, to our knowledge, to compare our FeSb AFM results, there are calculations on the FM state available—the FM results between these are in qualitative agreement, however they have smaller magnetic moments due to the implementation of different functionals in the calculations [54]. While both the FeSb and FeTe₂ 1*T*-phase are AFM, we do not observe FeSb-type structures

TABLE III. Ground-state energies (eV/F.U.).

	IP AFM	OP AFM	FM	NM
FeSb	0.0000	0.1292	0.0986	0.4113
FeSb ₂ 1T	0.0643	0.0208	0.0000	0.5368
FeSb ₂ 2H	0.0138	0.0430	0.0000	0.3399
FeTe	0.0014	0.1116	0.0000	0.9172
FeTe ₂ 1T	0.0000	0.1119	0.0554	0.3068
FeTe ₂ 2H	0.1393	0.0105	0.0000	0.4586
NiTe ₂ 1T	Unstable	Unstable	0.0003	0.0000

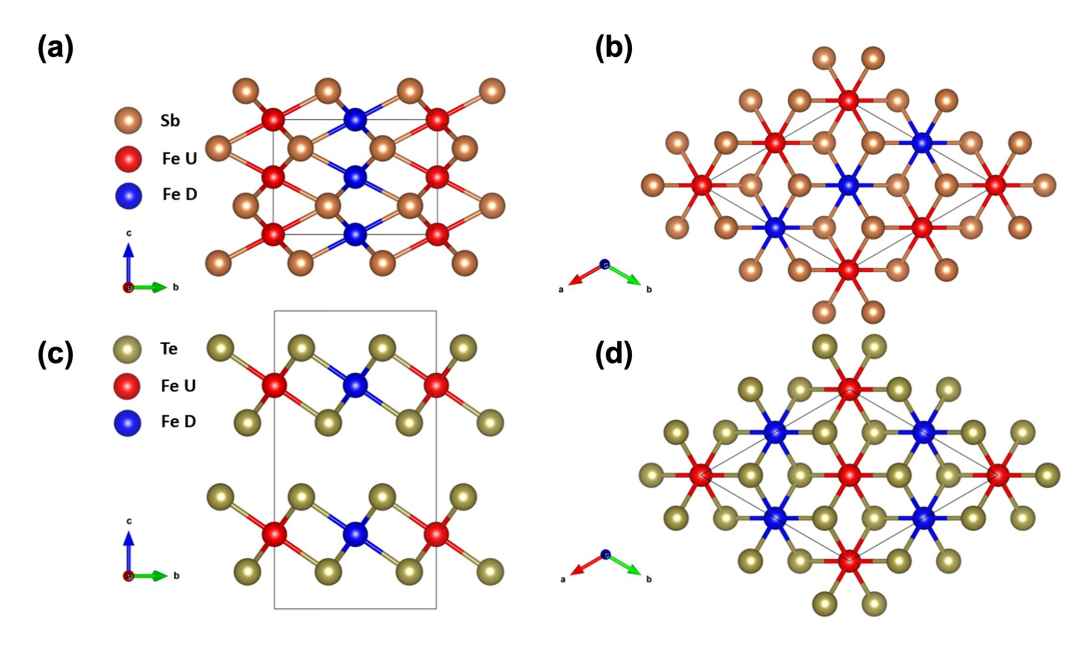


FIG. 6. (a) The crystal structures of FeSb (a),(b) and FeTe₂ 1T (c),(d) are shown from along the a-lattice vector (a),(c) and the c-lattice vector (b),(d). The red and blue atoms represent spin-up and spin-down Fe atoms, respectively, depicting the FM coupling between layers (a),(c) and the "stripe" -type AFM coupling (b),(d) within layers.

in our HAADF-STEM images, therefore we have determined that the AFM interfacial phase present at the Sb₂Te₃/Py interface is consistent with the FeTe₂ 1*T*-phase.

IV. CONCLUSIONS

In conclusion we have studied the Sb₂Te₃/Py heterostructure and, with low temperature magnetometry, discovered a large exchange bias which indicates the presence of FM/AFM exchange coupling. The HAADF-STEM and EELS materials characterization revealed Fe and Ni diffusion into the Sb₂Te₃ film, yielding the secondary phase formation of a NiTe₂ 1T-type structural phase. From first-principles calculations performed for structures of XY, XY_2 1T, and XY_2 2H (X = Ni, Fe and Y = Te, Sb), we found that NiTe₂ 1T had no stable AFM solutions, whereas FeSb and FeTe₂ 1T-phase are AFM. While there is theoretical support that FeSb and FeTe₂ 1T are AFM, based on our HAADF-STEM results, there is strong justification that the interfacial phase at the Sb₂Te₃/Py interface is consistent with the FeTe₂ 1T-phase. We must note that the precise chemistry of the interfacial phase could not be determined, therefore it is possible that the FeTe₂ 1T and/or an intermixed $(Fe_{1-x}Ni_x)Te_2$ 1*T*-phase is present at the interface contributing to the AFM/FM exchange coupling. From Fig. 3(d) the derivative of the ZFC curve is a bit broad which may indicate the AFM phase transition is smeared out with temperature. We believe that along with FeTe₂ 1T-phase that there is likely the existence of some $(Fe_{1-x}Ni_x)Te_2 1T$ -phase and that this nickel incorporation into the structure will most certainly alter the phase transition temperature. It is also important to emphasize that we have performed calculation only on hexagonal structures, therefore we did not explicitly study the tetragonal phase of FeTe, which is a known antiferromagnet [55,56]. While this tetragonal FeTe phase is not evident in our STEM images, it cannot be completely ruled out here. It is possible FeTe₂ 1T-type phase is the prominent phase, but there could be traces of tetragonal FeTe that we could not explicitly identify here. Overall, this study has demonstrated that novel metastable phases may be formed at TI/FM interfaces, which should be the subject of further studies, because they may lead to the discovery of new magnetic and/or topological materials. Along with the discovery of the AFM interfacial material consistent with the intermixed (Fe, Ni)Te₂ 1T-phase, the interface was found to have significant disorder such as stacking faults and an inhomogeneous interface. Additional, magnetic signatures of disorder were observed namely that the coercive field dependence and the exchange bias dependence are slightly different. We attribute the coercive field temperature dependence to the presence of a magnetically frustrated interface leading to pinned domains that will contribute to the total switching energy. It is not a reach to assume this, because from the STEM imaging we can conclude the interface is highly inhomogeneous and rough which may influence magnetic frustration near the interface. Despite the magnetically frustrated interface and the formation of the FeTe₂ 1T-type phase at the Sb₂Te₃/Py interface, we still found evidence of spin-pumping in this system (significant enhancement in Gilbert damping accompanied by decrease in effective magnetization in-plane). This highlights that despite these mixed interfaces, heterostructures can still be used in spin-orbit-torque memory applications. However, it may be useful to mitigate this mixed interface formation by introducing a spacer layer such as Ag, or Ti [40,57-60]. More studies should be conducted about whether the spinpumping effect is enhanced by the presence of an additional AFM phases at the interface of TI/FM heterostructures. While this work focused on the FM/AFM exchange coupling between permalloy and the interfacial AFM phase formed at the interface with Sb₂Te₃ there has been other interesting research directions focused on AFM/TI coupled interactions in literature. These exotic interactions range from interfacial superconductivity (Bi₂Te₃/FeTe) [61] to AFM-induced magnetic proximity effect in TI with potential to exhibit quantum anomalous Hall effect [62–64].

ACKNOWLEDGMENTS

A.R.W.-C., N.B., N.X.S., S.K.P., and S.H.T. acknowledge financial support from NSF TANMS ERC under Award No. 1160504. A.R.W.-C. was supported by the National Defense Science and Engineering Graduate Fellowship of the Office of Naval Research. J.L.H. was supported by the Gordon and Betty Moore Foundation EPiOS Synthesis Investigator

Award. This work was partially supported by the National Science Foundation Grant No. DMR-1905662 and the Air Force Office of Scientific Research Award No. FA9550-20-1-0247 (D.H.). M.M. and A.B. acknowledge the support of the support of the U.S. Department of Energy (DOE), Office of Science, Basic Energy Sciences Grant No. DE-SC0022216 (accurate modeling of complex magnetic states), and they benefited from Northeastern University's Advanced Scientific Computation Center and the Discovery Cluster and the National Energy Research Scientific Computing Center through DOE Grant No. DE-AC02-05CH11231.

The authors do not have any conflicts of interest to declare.

- [1] A. Bansil, H. Lin, and T. Das, Rev. Mod. Phys. **88**, 021004 (2016).
- [2] M. Z. Hasan and C. L. Kane, Rev. Mod. Phys. 82, 3045 (2010).
- [3] N. P. Armitage, E. J. Mele, and A. Vishwanath, Rev. Mod. Phys. 90, 015001 (2018).
- [4] Y. Cao, G. Xing, H. Lin, N. Zhang, H. Zheng, and K. Wang, iScience 23, 101614 (2020).
- [5] A. R. Mellnik, J. S. Lee, A. Richardella, J. L. Grab, P. J. Mintum, M. H. Fisher, A. Vaezi, A. Manchon, E.-A. Kim, N. Samarth, and D. C. Ralph, Nature (London) 511, 449 (2014).
- [6] D. C. M., R. Grassi, J. Y. Chen, M. Jamali, D. Reifsnyder Hickey, D. Zhang, Z. Zhao, H. Li, P. Quarterman, Y. Lv et al., Nat. Mater. 17, 800 (2018).
- [7] N. H. D. Khang, Y. Ueda, and P. N. Hai, Nat. Mater. 17, 808 (2018).
- [8] Q. Lu, P. Li, Z. Guo, G. Dong, B. Peng, X. Zha, T. Min, Z. Zhou, and M. Liu, Nat. Commun. 13, 1650 (2022).
- [9] M. Jamali, J. S. Lee, J. S. Jeong, F. Mahfouzi, Y. Lv, Z. Zhao, B. K. Nikolić, K. Andre Mkhoyan, N. Samarth, and J.-P. Wang, Nano Lett. 15, 7126 (2015).
- [10] Y. Deng, M. Yang, Y. Ji, and K. Wang, J. Magn. Magn. Mater. 496, 165920 (2020).
- [11] Y. Tokura, K. Yasuda, and A. Tsukazaki, Nat. Rev. Phys. 1, 126 (2019).
- [12] A. J. Bestwick, E. J. Fox, X. Kou, L. Pan, K. L. Wang, and D. Goldhaber-Gordon, Phys. Rev. Lett. 114, 187201 (2015).
- [13] C. Z. Chang, W. Zhao, D. Kim, H. Zhang, B. A. Assaf, D. Heiman, S.-C. Zhang, C. Liu, M. H. W. Chan, and J. S. Moodera, Nat. Mater. 14, 473 (2015).
- [14] J.-M. Zhang, W. Zhu, Y. Zhang, D. Xiao, and Y. Yao, Phys. Rev. Lett. 109, 266405 (2012).
- [15] C. Liu, Y. Wang, M. Yang, J. Mao, H. Li, Y. Li, J. Li, H. Zhu, J. Wang, L. Li *et al.*, Nat. Commun. **12**, 4647 (2021).
- [16] K. He, npj Quantum Mater. 5, 90 (2020).
- [17] P. Wei, F. Katmis, A. Badih, A. Assaf, H. Steinberg, P. Jarillo-Herrero, D. Heiman, and J. S. Moodera, Phys. Rev. Lett. 110, 186807 (2013).
- [18] M. Lang, M. Montzeri, M. C. Onbasli, X. Kou, Y. Fan, P. Upadhyaya, K. Yao, F. Liu, Y. Jiang, W. Jiang *et al.*, Nano Lett. **14**, 3459 (2014).
- [19] F. Katmis, V. Lauter, F. Nogueira, B. A. Assaf, M. E. Jamer, P. Wei, B. Satpato, J. W. Freeland, I. Eremin, D. Heiman, P. Jarillo-Herrero, and J. S. Moodera, Nature (London) 533, 513 (2016).

- [20] T. Liu, J. Kally, T. Pillsbury, C. Liu, H. Chang, J. Ding, Y. Cheng, M. Hilse, R. Engel-Herbert, A. Richardella, N. Samarth, and M. Wu, Phys. Rev. Lett. 125, 017204 (2020).
- [21] L. J. Riddiford, A. J. Grutter, T. Pillsbury, M. Stanley, D. Reifsnyder Hickey, P. Li, N. Alem, N. Samarth, and Y. Suzuki, Phys. Rev. Lett. 128, 126802 (2022).
- [22] M. D. Davydova, A. S. Pakhomov, A. N. Kuz'michev, P. M. Vetoshko, P. N. Skirdkov, H. C. Han, Y. S. Chen, J. G. Lin, J. C. Wu, J. C. A. Huang, and K. A. Zvezdin, J. Elect. Mater. 48, 1375 (2019).
- [23] A. Baker, A. Figueroa, L. Collins-McIntyre, G. van der Laan, and T. Hesjedal, Sci. Rep. 5, 7907 (2015).
- [24] C. D. Spataru and F. Leonard, Phys. Rev. B 90, 085115 (2014).
- [25] W. Ye, A. B. Pakhomov, S. Xu, H. Lu, Z. Wu, Y. Han, T. Han, Y. Wu, G. Long, J. Lin *et al.*, arXiv:1511.03421 (2015).
- [26] L. A. Walsh, C. M. Smyth, A. T. Barton, Q. Wang, Z. Che, R. Yue, J. Kim, M. J. Kim, R. M. Wallace, and C. L. Hinkle, J. Phys. Chem. C 121, 23551 (2017).
- [27] S.-J. Chang, P.-Y. Chuang, C.-W. Chong, Y.-J. Chen, J. C.-A. Huang, P.-W. Chen, and Y.-C. Tseng, RSC Adv. 8, 7785 (2018).
- [28] N. Bhattacharjee, K. Mahalingam, A. Fedorko, V. Lauter, M. Matzelle, B. Singh, A. Grutter, A. R. Will-Cole, M. Page, M. McConney, R. Markiewicz, A. Bansil, D. Heiman, and N. X. Sun, Adv. Mater. 34, 2108790 (2022).
- [29] M. Yan, H. Huang, K. Zhang, E. Wang, W. Yao, K. Deng, G. Wan, H. Zhang, M. Arita, H. Yang *et al.*, Nat. Commun. 8, 257 (2017).
- [30] C. Xu., B. Li, W. Jiao, W. Zhou, B. Qian, R. Sankar, N. D. Zhigadlo, Y. Qi, D. Qian, F.-C. Chou, and X. Xu, Chem. Mater. 30, 4823 (2018).
- [31] S. Chen, H. Liu, F. Chen, K. Zhou, and Y. Xue, ACS Nano 14, 11473 (2020).
- [32] H. Wu, Z. Feng, A. Pal, H. Dong, C. Jing, K. Wang, S. Zhang, W. Deng, S. Li, J. Feng *et al.*, Chem. Mater. 33, 4927 (2021).
- [33] A. Podpirka, J. Gagnon, C. Zgrabik, J. Pierce, and D. Shrekenhamer, J. Vac. Sci. Technol. B 38, 032210 (2020).
- [34] See Supplemental Material at http://link.aps.org/supplemental/ 10.1103/PhysRevMaterials.7.024406 for additional images/ data.
- [35] K. Hoefer, C. Becker, S. Wirth, and L. H. Tjeng, AIP Adv. 5, 097139 (2015).
- [36] S. Mizukami, Y. Ando, and T. Miyazaki, Jpn. J. Appl. Phys. 40, 580 (2001).

- [37] M. Morota, Y. Saito, and N. Uchida, Phys. Status Solidi RRL, **15** 2100247 (2021).
- [38] Y. Chen, X. Gu, Y. Li, X. Du, L. Yang, and Y. Chen, Matter 3, 1114 (2020).
- [39] C. Tang, Q. Song, C.-Z. Chang, Y. Xu, Y. Ohnuma, M. Matsuo, Y. Liu, W. Yuan, Y. Yao, J. S. Moodera, S. Maekawa, W. Han, and J. Shi, Sci. Adv. 4, eaas8660 (2018).
- [40] K. Kondou, R. Yoshimi, A. Tsukazaki, Y. Fukuma, J. Matsuno, K. S. Takahashi, M. Kawasaki, Y. Tokura, and Y. Otani, Nat. Phys. 12, 1027 (2016).
- [41] J. Nogués and I. K. Schuller, J. Magn. Magn. Mater. 192, 203 (1999).
- [42] J. Li, Y. Li, S. Du, Z. Wang, B.-L. Gu, S.-C. Zhang, K. He, W. Duan, and Y. Xu, Sci. Adv. 5, eaaw5685 (2019).
- [43] The Materials Project. Materials Data on NiTe₂ by Materials Project. United States, https://doi.org/10.17188/1200993.
- [44] E. J. Kirkland, Advanced Computing in Electron Microscopy (Plenum, New York, 1998).
- [45] G. Kresse and D. Joubert, Phys. Rev. B **59**, 1758 (1999).
- [46] G. Kresse and J. Hafner, Phys. Rev. B 47, 558 (1993).
- [47] G. Kresse and J. Hafner, Phys. Rev. B 49, 14251 (1994).
- [48] G. Kresse and J. Furthmüller, Comput. Mater. Sci. 6, 15 (1996).
- [49] G. Kresse and J. Furthmüller, Phys. Rev. B 54, 11169 (1996).
- [50] M. Aras, Ç. Kılıç, and S. Ciraci, Phys. Rev. B 101, 054429 (2020).
- [51] J. Sun, A. Ruzsinszky, and J. P. Perdew, Phys. Rev. Lett. 115, 036402 (2015).
- [52] C. Lane, J. W. Furness, I. G. Buda, Y. Zhang, R. S. Markiewicz, B. Barbiellini, J. Sun, and A. Bansil, Phys. Rev. B 98, 125140 (2018).
- [53] J. Sun, R. C. Remsing, Y. Zhang, Z. Sun, A. Ruzsinszky, H.

- Peng, Z. Yang, A. Paul, U. Waghmare, X. Wu, M. L. Klein, and J. P. Perdew, Nat. Chem. 8, 831 (2016).
- [54] A. Jain, S. P. Ong, G. Hautier, W. Chen, W. Davidson Richards, S. Dacek, S. Cholia, D. Gunter, D. Skinner, G. Ceder, and K. A. Persson, APL Mater. 1, 011002 (2013).
- [55] E. E. Rodriguez, C. Stock, P. Zajdel, K. L. Krycka, C. F. Majkrazak, P. Zavalij, and M. A. Green, Phys. Rev. B 84, 064403 (2011).
- [56] C. Trainer, M. Songvilay, N. Qureshi, A. Stunault, C. M. Yim, E. E. Rodriguez, C. Heil, V. Tsurkan, M. A. Green, A. Loidl, P. Wahl, and C. Stock, Phys. Rev. B 103, 024406 (2021).
- [57] V. Sharma, W. Wu, P. Bajracharya, D. Q. To, A. Johnson, A. Janotti, G. W. Bryant, L. Gundlach, M. B. Jungfleisch, and R. C. Budhani, Phys. Rev. Mater. 5, 124410 (2021).
- [58] N. Bhattacharjee, K. Mahalingam, A. Will-Cole, Y. Wei, A. Fedorko, C. T. Bowers, M. Page, M. McConney, D. Heiman, and N. X. Sun, Adv. Mater. Interfaces 9, 2201691 (2022).
- [59] F. Bonell, M. Goto, G. Sauthier, J. F. Sierra, A. I. Figueroa, M. V. Costache, S. Miwa, Y. Suzuki, and S. O. Valenzuela, Nano Lett. 20, 5893 (2020).
- [60] H. Wu, P. Zhang, P. Deng, Q. Lan, Q. Pan, S. A. Razavi, X. Che, L. Huang, B. Dai, K. Wong, X. Han, and K. L. Wang, Phys. Rev. Lett. 123, 207205 (2019).
- [61] Q. L. He, H. Liu, M. He, Y. H. Lai, H. He, G. Wang, K. T. Law, R. Lortz, J. Wang, and I. K. Sou, Nat. Commun. 5, 4247 (2014).
- [62] Q. L. He, X. Kou, A. J. Grutter, G. Yin, L. Pan, X. Che, Y. Liu, T. Nie, B. Zhang, S. M. Disseler *et al.*, Nat. Mater. 16, 94 (2017).
- [63] Y. Liu, X. Niu, R. Zhang, Q. Zhang, J. Teng, and Y. Li, Chin. Phys. Lett. 38, 5 (2021).
- [64] P. Liu, C. Eckberg, L. Pan, P. Zhang, K. L. Wang, and G. Lüpke, Sci. Rep. 12, 12117 (2022).